RSC Advances

ROYAL SOCIETY OF CHEMISTRY

www.rsc.org/advances

Journal Name

ARTICLE

Influence of Transition Metal (M = Co, Fe and Mn) on Ordered Mesoporous CuM/CeO_2 and Catalytic application in Selective Catalytic Reduction of NO_x with H_2

Received 00th January 20xx,
Accepted 00th January 20xx

DOI: 10.1039/x0xx00000x

www.rsc.org/

Xiuyun Wang,[a] Wu Wen,[a,b] Yanqing Su[a,b] and Ruihu Wang*[a]

A series of ordered mesoporous Cu/CeO_2 and CuM/CeO_2 (M = Fe, Co and Mn) were synthesized using mesoporous KIT-6 as a hard template. These materials were characterized by XRD, N_2 physisorption, Raman, TEM, XPS, H_2-TPR and NO-TPD. N_2 physisorption has demonstrated that Cu/CeO_2 and CuM/CeO_2 possess high surface area of 146-193 m^2/g and narrow pore size distribution of 3-8 nm. XRD and Raman analyses show that Ce-M(Cu)-O solid solution is formed in CuM/CeO_2. The surface CoO_x species are also observed in CuCo/CeO_2. NO-TPD and XPS analyses reveal that CuCo/CeO_2 possesses lower NO desorption temperature and more oxygen vacancies. Their application in selective catalytic reduction of NO_x with H_2 in the presence of oxygen was evaluated. CuCo/CeO_2 shows wide temperature window and high NO_x conversion of more than 80% at 200 °C.

Introduction

Nitrogen oxides (NO_x) are mainly emitted from automobile exhaust gas and industrial combustion of fossil fuels, which are hazardous to environment and human health.[1-3] Several promising catalytic technologies including NO_x storage and reduction (NSR) and selective catalytic reduction (SCR) have been developed to reduce NO_x emission.[2-7] Among them, SCR of NO_x with either hydrocarbons (HC-SCR) or ammonia/urea (NH_3-SCR) is an effective method in the treatment of industrial flue gas.[5-7] V_2O_5-WO_3 (MO_3)/TiO_2 are widely used as commercial NH_3-SCR catalysts. However, practical application of these vanadia-based catalysts has been restrained in diesel engines due to inevitable problems, such as toxicity of vanadium, SO_2 affinity, over-oxidation of NH_3 to N_2O, and employment within a narrow temperature window of 300-400 °C.[8] Therefore, it is highly desirable to develop alternative catalysts, which are supposed to be non-toxic, inexpensive and high efficiency at low temperature.

Recently, SCR of NO_x with H_2 (H_2-SCR) has attracted more and more attention in NO_x removal because NO_x can be efficiently reduced at low temperature (T < 200 °C). In addition, the combustion of H_2 in air produces water, making it more environmentally benign.[9] However, most of H_2-SCR catalysts are noble metal-supported catalysts,[10, 11] high cost of precious metals and their sensitivity to sulfur poisoning have inhibited their large-scale applications. The search for precious metal-substituted catalysts is of great significance.

Transition metal oxides have been of considerable interest in heterogeneous catalysis owing to their ready synthesis, low price and good redox property. Among them, Fe_3O_4, Co_3O_4, MnO_2, NiO and CuO_x have been extensively investigated in SCR of NO_x.[12, 13] To improve the activity and enhance the stability of these transition metal catalysts,[14] CeO_2 is often used as a support due to its high oxygen storage capacity and rich oxygen vacancies.[15,16] Recently, high degree of dispersion and facile redox interplay between Cu and Ce are proposed to enhance catalytic activity of Cu/CeO_2 catalysts,[17] Cu-O_v-Ce interface is thought to be responsible for their low temperature redox properties.[18] Many synthetic methods, such as co-precipitation, impregnation, ion exchange, homogeneous deposition-preparation and sol-gel method,[17-20] have been developed for the preparation of CuO/CeO_2 catalysts, but these catalysts usually possess low surface area owing to the blocking of partial pores and growth of CeO_2 crystallites in the process of their synthesis. One of the effective methods to enhance surface area of metal oxides is nanocasting route using KIT-6 as a hard template.[20] The cubic I_{a3d} symmetry and two interpenetrating branched networks of cylindrical pores in KIT-6 may endow the resultant materials particular advantages, such as ordered mesoporous structure, narrow pore size distribution and adjustable porous properties, which are beneficial to improve their catalytic performance. In addition, multi-metal oxides are widely used as SCR catalysts because they can provide superior general properties through

[a] State Key Laboratory of Structural Chemistry, Fujian Institute of Research on the Structure of Matter, Chinese Academy of Sciences, Fuzhou, Fujian, 350002, China. E-mail: ruihu@fjirsm.ac.cn
[b] College of Materials Science and Engineering, Fujian Normal University, Fuzhou, Fujian, 350007, China.
Electronic Supplementary Information (ESI) available: [N_2 selectivity, stability test and SO_2 poisoning test]. See DOI: 10.1039/x0xx00000x

synergetic interactions of different compositions.[7] The use of ordered mesoporous multi-metal oxide catalysts can be expected to show good SCR performances. However, to the best of our knowledge, the preparation of ordered mesoporous Cu/CeO_2 catalysts containing other transition metal oxides and application in SCR of NO_x have not been reported hitherto. In our continuous efforts to develop low-temperature and SO_2-tolerant SCR catalysts, [21,22] herein, we report a series of ordered mesoporous CuM/CeO_2 catalysts (M = Fe, Co and Mn). These catalysts show superior NO_x conversion, high N_2 selectivity and good stability in SCR of NO_x with H_2.

Experimental

Catalysts preparations

$Cu(NO_3)_2{\cdot}6H_2O$, $Co(NO_3)_2{\cdot}6H_2O$ and $Ce(NO_3)_2{\cdot}6H_2O$ (total mass: 1 g) with quality ratio of Cu: Ce: Co = 1:7:2 were dissolved in ethanol (15 mL). After the solution was stirred at room temperature for 1h, 0.5g of KIT-6 (purchased from nano-science and technology companies in Nanjing) was added. The suspension was stirred at room temperature for 24 h, dried at 120 °C overnight, and followed by calcination at 400 °C for 4 h. The obtained sample was denoted as $CuCo/CeO_2$. Mesoporous $CuMn/CeO_2$ (quality ratio of Cu:Ce:Mn = 1:7:2), $CuFe/CeO_2$ (quality ratio of Cu:Ce:Fe = 1:7:2) and Cu/CeO_2 (quality ratio of Cu:Ce = 1:9) were prepared by similar procedures using different salt nitrates.

Catalytic activity tests

SCR activity measurement was performed in a fixed-bed stainless steel reactor (inner diameter = 8 mm). Before each test, a 0.4 g of 20-30 mesh sample was reduced by 3.5 vol% H_2/Ar at 500 °C for 2 h. After cooled to test temperature, the feed gas (450 ppm NO, 1.5 vol% H_2 and 2 vol% O_2 balanced with Ar) was introduced using mass-flow controllers at a total flow rate of 500 mL/min, giving corresponding GHSV at 75,000 h^{-1}. SO_2 poisoning experiment was performed by exposing samples to feed gas containing the additional 100 ppm SO_2 at 100-400 °C. Outlet NO_x concentration was monitored by an on-line chemiluminescence $NO\text{-}NO_2\text{-}NO_x$ analyzer (Model 42i-HL, Thermo Scientific). The N_2 selectivity was analyzed using a GC 7820A.NO_x conversion was calculated until a steady state was achieved at the given temperature for 45 min. Stability test of $CuCo/CeO_2$ and Cu/CeO_2 was performed in the presence of 450 ppm NO, 1.5 vol% H_2/Ar and 2 vol% O_2/Ar balanced with Ar at 390 °C.

Characterizations

Powder X-ray diffraction (XRD) was performed on a Rigaku-DMax2500PC diffractometer using a Cu-K_α radiation (λ = 1.5406 Å). N_2 physisorption measurement was performed on an ASAP 2020 apparatus, the sample was degassed in vacuo at 180 °C at least 6 h before the measurement. H_2 temperature-programmed reduction (H_2-TPR) was performed on AutoChem II 2920 equipped with a TCD, in which the catalysts were pretreated under air flow (30 mL/min) at 500 °C for 0.5 h, followed by purging with Ar (30 mL/min) at the same temperature for 0.5 h. After cooling to room temperature, the temperature was increased at 5 °C/min up to 800 °C by a temperature-programmed controller in a gas flow of 10 vol% H_2/Ar (30 mL/min). NO-TPD was performed on AutoChem II 2920 equipped with a TCD detector. A sample of 0.1 g was pretreated in 8% O_2/Ar at 350 °C for 1h with a flow rate of 50 mL/min. After cooled to room temperature, the sample was exposed to a mixture gas of 500 ppm NO and Ar as balance (Total gas flow rate: 50 mL/min) for 1 h and then subsequently flushed with 8 % O_2/Ar to remove weakly absorbed NO species. NO-TPD experiment was carried out from room temperature to 600 °C at 10°C/min. For the analysis of the gases evolving in the NO-TPD quadruple mass spectroscopy (Q-MS) was used. The signals for NO (m/e = 30), N_2 (m/e = 28), N_2O (m/e = 44), NH_3 (m/e = 17) and NO_2 (m/e = 46) were monitored by a QIC-20 bench top gas analysis system connected to an AutoChemII 2920 outlet. X-ray photoelectron spectroscopy (XPS) analysis was performed on Physical Electronics Quantum 2000, equipped with a monochromatic Al-K_α source (K_α = 1,486.6 eV) and a charge neutralizer. Transmission Electron Microscope (TEM) and high-resolution transmission electron microscopy (HRTEM) measurements were carried out on a JEM-2010 microscope operating at 200 kV in the mode of bright field. Raman spectra were collected by using a Renishaw Invia system at RT. Diffuse reflectance UV-vis spectra were collected on a Perkin Elmer Lambda 950 spectrophotometer equipped with an integrating sphere in the range from 200 and 800 nm using $BaSO_4$ as a reference.

Results and Discussion

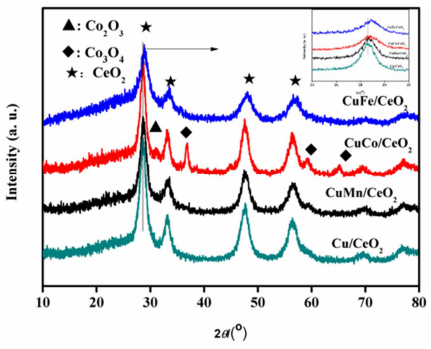

Fig. 1 XRD patterns of Cu/CeO_2 and CuM/CeO_2.

To identify structures of as-prepared samples, XRD patterns and Raman spectra of Cu/CeO_2 and CuM/CeO_2 were investigated. As shown in Fig. 1, there are four main diffraction peaks at 28.64, 33.24, 47.92 and 56.42° in XRD pattern of Cu/CeO_2, which can be indexed as (111), (200), (220) and (311), respectively, corresponding to lattice planes of cubic CeO_2.[23]

comparison with Cu/CeO_2, the main diffraction peaks in CuM/CeO_2 are slightly shifted to higher 2θ owing to lattice contraction. It should be mentioned that no phases of Cu species are observed in all of samples, suggesting that Cu species are finely dispersed on the support or they are incorporated into CeO_2 framework to form a solid solution.[24] The detectable diffraction peaks of Fe and Mn species are also not found, which is probably attributed to the incorporation of Fe and Mn cations into ceria framework to form a Ce-M-O solid solution. Notably, two types of the additional diffraction peaks of Co_2O_3 (2θ = 31.26 °) and Co_3O_4 (2θ = 36.8, 59.32 and 65.20 °) phases are observed in $CuCo/CeO_2$, indicating that partial CoO_x species are formed on the surface, which may provide more sites for NO_x adsorption.[23] The lattice parameter (a_{111}) and crystallite size of Cu/CeO_2 and CuM/CeO_2 are calculated based on Bragg's law and Scherrer equation, respectively. As shown in Table 1, the lattice parameter in Cu/CeO_2 is 0.5407 nm, and the values are slightly decreased in CuM/CeO_2. It was reported that the existence of Ce-M-O solid solution may inhibit the growth of crystalline size of metal oxides and promote the activation of oxygen species,[25] which are favorable for the improvement of SCR activities. The crystalline sizes in (111) plane of cubic CeO_2 in $CuCo/CeO_2$, $CuMn/CeO_2$ and $CuFe/CeO_2$ are 30.6, 30.5 and 32.0 nm, respectively, which are smaller than that of Cu/CeO_2 (33.90 nm).

Table 1 Lattice parameter, crystalline size, textural properties and total NO desorption amounts of Cu/CeO_2 and CuM/CeO_2.

Sample	BET surface area(m^2/g)	Average pore radius(nm)	Pore volume (cm^3/g)	Lattice parameter(nm)	Total NO desorption amount (*m*mol/g)	Crystalline size(nm)
Cu/CeO_2	160	3.90	0.26	0.5407	1.03	33.9
$CuCo/CeO_2$	146	2.80	0.27	0.5355	1.39	30.6
$CuFe/CeO_2$	176	2.95	0.26	0.5344	1.35	32.0
$CuMn/CeO_2$	193	3.49	0.26	0.5397	1.69	30.5

XRD is related to the cationic sublattice, while Raman is dominated by oxygen lattice vibrations.[21] Raman spectroscopy is usually regarded as a potential tool to obtain the additional structure information of XRD patterns because it is sensitive to crystal symmetry. In order to further clarify structural characterization of Cu/CeO_2 and CuM/CeO_2, Raman spectra of Cu/CeO_2 and CuM/CeO_2 are presented in Fig. 2. Cu/CeO_2, $CuCo/CeO_2$ and $CuMn/CeO_2$ show a strong peak at 446 cm^{-1}, corresponding to F2g vibration mode of cubic fluorite structure.[26] However, the characteristic peak in $CuFe/CeO_2$ is shifted to 453 cm^{-1}. In comparison with pure CeO_2 (460 cm^{-1}), the peak in CuM/CeO_2 shifts toward a low frequency, further suggesting that lattice contraction because some of M cations are incorporated into CeO_2 lattice.[27] Notably, the peak intensity in $CuMn/CeO_2$ and $CuCo/CeO_2$ is stronger than that of Cu/CeO_2, while $CuFe/CeO_2$ shows the weakest peak intensity. Cu/CeO_2, $CuMn/CeO_2$ and $CuCo/CeO_2$ also possess a weak peak around 547, 568 and 575–cm^{-1}, respectively, which is ascribed to the presence of oxygen vacancies or lattice defects. It should be mentioned that these weak peaks shift to higher wavenumber at 620 cm^{-1} in $CuFe/CeO_2$, which is ascribed to the vacancy-interstitial oxygen defects in ceria.[18,23] These results suggest the oxygen defects in $CuFe/CeO_2$ are different from other samples. The formation oxygen vacancies mainly result from charge balance when Ce^{4+} is replaced by M^{n+} or Cu ions.[28] However, no clear peaks of M oxides are observed, one reason is that Raman bands in MO_x are much weaker than that of CeO_2 due to strong absorbance of CeO_2 at the wavenumber region of Raman spectra. The other is associated with the formation of Ce-M(Cu)-O solid solutions.[27] The ratio of the peak area at 547-620 cm^{-1} (A_2) to that at 446-453 cm^{-1} (A_1) is related to the degree of oxygen vacancies or defect sites, and a higher A_2/A_1 ratio usually means more defect sites,[29] which may result in better catalytic performances. As shown in Fig. 2b, A_2/A_1 ratio follows the sequence: $CuCo/CeO_2$ (11.26%) > $CuMn/CeO_2$ (10.09%) > Cu/CeO_2 (8.69%) > $CuFe/CeO_2$ (8.46%), demonstrating $CuCo/CeO_2$ possesses the most oxygen vacancies or defect sites.

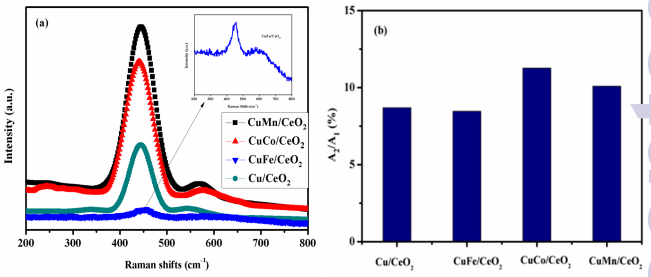

Fig. 2 Raman spectra (a) and the peak area ratio (b) for Cu/CeO_2 and CuM/CeO_2.

N_2 adsorption/desorption isotherms and corresponding BJH pore size distributions of Cu/CeO_2 and CuM/CeO_2 are shown in Fig. S1. Their isotherms exhibit type-IV pattern with H_2 hysteresis loop, suggesting the existence of mesoporous structure.[30-33] The specific surface areas and pore volume of Cu/CeO_2 and CuM/CeO_2 are in the range of 146-193 m^2/g and 0.26-0.27 cm^3/g, respectively (Table 1). The maximum value of pore size in Cu/CeO_2, $CuCo/CeO_2$ and $CuMn/CeO_2$ is around 3.2 nm, while it is at 2.9 nm for $CuFe/CeO_2$. Notably, Cu/CeO_2 and $CuMn/CeO_2$ possess the other pore sizes at 10.8 and 6.4 nm, which may be attributed to bi-modal pore size distribution.

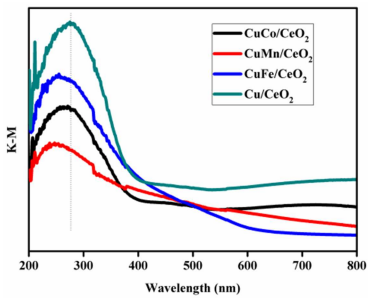

Fig. 3 UV-vis spectra of Cu/CeO_2 and CuM/CeO_2.

To further investigate structural properties of Cu/CeO_2 and CuM/CeO_2, their UV-vis spectra were examined. As shown in Fig. 3, there is a strong band at 200-300 nm in Cu/CeO_2 and CuM/CeO_2, which may be assigned to charge transfer between O^{2-} and Ce^{4+}. In comparison with Cu/CeO_2, an obvious redshift occurs in CuM/CeO_2, which is attributed to charge transfer between d-electrons of transition metal ions and CeO_2 valence band. In addition, the absorbance intensity of CuM/CeO_2 is weaker than that of Cu/CeO_2. These observations suggests the increment of oxygen vacancies in CuM/CeO_2 due to the charge compensation.

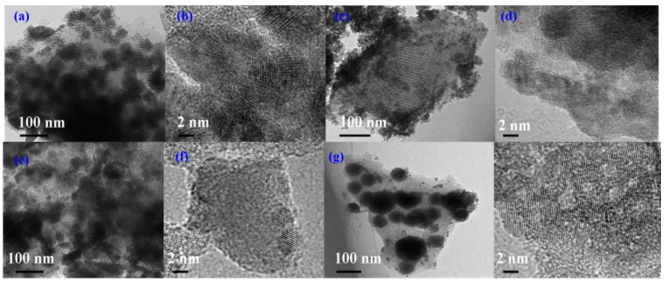

Fig. 4 TEM images for fresh (a) $CuCo/CeO_2$, (c) $CuMn/CeO_2$, (e) $CuFe/CeO_2$ and (g) Cu/CeO_2; HR-TEM of (b) $CuCo/CeO_2$, (d) $CuMn/CeO_2$, (f) $CuFe/CeO_2$ and (h) Cu/CeO_2.

TEM images of fresh Cu/CeO_2 and CuM/CeO_2 are shown in Fig. 4. All catalysts show the ordered mesoporous structures, the ordered arrangement of oxide particles can be clearly observed. The diameter of CuM/CeO_2 particles is around 9 nm, which is close to the pore size of KIT-6 template (10 nm), suggesting that the pore channels of KIT-6 silica confine the growth of the catalyst seeds in a limited space. Moreover, the lattice fringes can be clearly observed in their high-resolution TEM (HR-TEM), suggesting highly crystalline nature of these mesoporous catalysts. The lattice fringe of CuM/CeO_2 is 0.31±0.02 nm, corresponding to (111) plane of CeO_2 or Ce-M(Cu)-O solid solution.

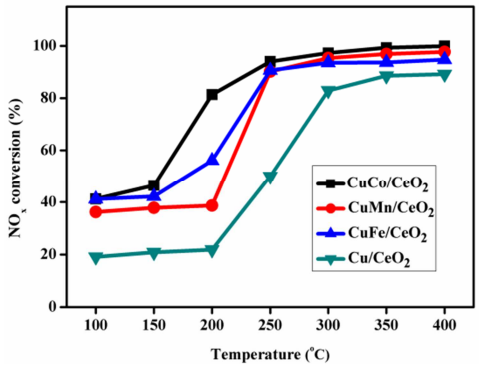

Fig.5 NO_x conversion of Cu/CeO_2 and CuM/CeO_2.

The catalytic activities of Cu/CeO_2 and CuM/CeO_2 in SCR of NO_x are presented in Fig. 5. For Cu/CeO_2 and $CuMn/CeO_2$, NO_x conversions have no obvious change at 100-200 °C, and become to significantly increase from 200 to 250 °C, and then gradually reach the maximum of 89 and 96% at 350 °C respectively. NO_x conversions in $CuCo/CeO_2$ and $CuFe/CeO_2$ at 100-150 °C are increased slightly, a quick increment occurs from 150 to 200 °C, the maximum values are achieved at 350-400 °C. Notably, NO_x conversion in CuM/CeO_2 is higher than that of Cu/CeO_2 at 100-400 °C, especially at low temperature. For instance, NO_x conversions at 200 °C in $CuCo/CeO_2$, $CuFe/CeO_2$ and $CuMn/CeO_2$ are 80, 50 and 38%, respectively. The difference of SCR activity in CuM/CeO_2 may be related to the effects of 3d structure in transition metal ions on NO oxidation ability. It was reported that transition metal cations with d_0, d_5 (such as Fe_2O_3) and d_{10} electronic configurations are very stable because their crystal field stabilization energy (CFSE) is very low, leading to low ability of NO oxidation. However, high CFSE of $d_{6.7}$ configurations in Co_3O_4,[34] may facilitate electronic interaction with NO molecules, thus contributing to enhance SCR activity. In addition, excellent SCR activity in $CuCo/CeO_2$ is also related to surface CoO_x species, which may provide more sites for NO_x chemisorption. It should be mentioned that NO_x conversion in CuM/CeO_2 is more than 90% at 250-400 °C. Moreover, N_2 selectivity maintains more than 79% at 100-400 °C in $CuCo/CeO_2$ (Fig. S2). The stability was also tested. As shown in Fig. S3, NO_x conversions have no obvious variation in $CuCo/CeO_2$ and Cu/CeO_2 at 390 °C for 14 h.

It was well known that sulfur poisoning at low temperature mainly results from the competitive adsorption between SO_2 and NO_x on the active sites of the catalysts, while the deactivation at high temperature is ascribed to the formation of sulfites/sulfates at high temperature. $CuCo/CeO_2$ is chosen to investigate sulfur poisoning due to its superior SCR activity, and Cu/CeO_2 is also examined for comparison. As shown in Fig. S4, the presence of 100 ppm SO_2 results in a quick decrement of NO_x conversion at low temperature (100-250 °C), while a slight decrement occurs at 300-400 °C. For example, NO_x conversions in $CuCo/CeO_2$ and Cu/CeO_2 at 250 °C are decreased from 93 to 68% and from 50 to 17%, respectively, while they slightly lowered to 98 and 82% at 400 °C, respectively. These results suggest the addition of Co is helpful for inhibiting SO_2 poisoning at low temperature.

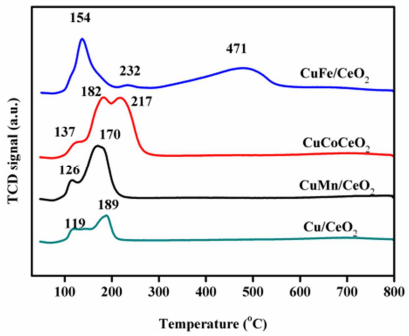

Fig. 6 H_2-TPR profiles of Cu/CeO_2 and CuM/CeO_2.

To further understand the effects of Fe, Co and Mn addition on SCR activities, the reducibility of Cu/CeO_2 and

CuM/CeO_2 are characterized by H_2-TPR, and the results are illustrated in Fig. 6. Two broad reduction peaks at 119and 189 ^oC are observed in Cu/CeO_2, which are attributed to the reduction of CuO species interacting with ceria surface and bulk CuO species to Cu^+ or Cu^0, respectively.[33] The first reduction peak in $CuMn/CeO_2$, $CuFe/CeO_2$ and $CuCo/CeO_2$ is increased to 126, 154 and 137 ^oC, respectively, which is ascribed to more negative free energy of formation of M oxides than that of Cu oxide, resulting in a lower reducibility. Notably, $CuCo/CeO_2$ and $CuFe/CeO_2$ have one additional peak at 217 and 232 ^oC, respectively, which is attributed to the reduction of Cu^+ species. However, such peak is not observed in $CuMn/CeO_2$, which may be attributed to the overlapping of reduction peaks between Cu ions and Mn ions.[34] Notably, there is a high reduction temperature at 471 ^oC in $CuFe/CeO_2$, corresponding to the reduction of Fe_2O_3 to Fe_3O_4.[35]

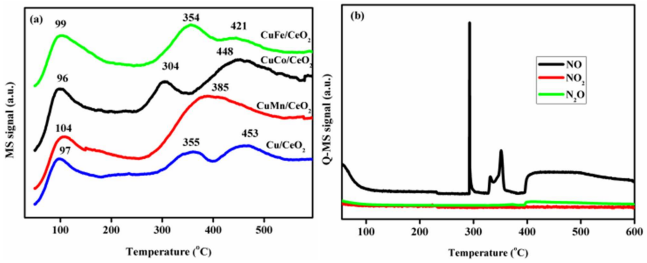

Fig. 7 (a) NO-TPD profiles of Cu/CeO_2 and CuM/CeO_2; (b) Q-MS of gases from NO-TPD in $CuCo/CeO_2$.

The adsorption behavior of NO is known to substantially affect SCR performances.[36] NO-TPD experiments were carried out in order to determine the adsorption capacity of NO in Cu/CeO_2 and CuM/CeO_2. As shown in Fig. 7a, three NO desorption peaks are observed in Cu/CeO_2, $CuFe/CeO_2$ and $CuCo/CeO_2$. For Cu/CeO_2, the desorption peaks at 97, 355 and453^oC are attributed to desorption of NO_x, surface adsorbed nitrite/nitrate and bulk nitrate species, respectively.[37] The addition of Co results in the decrement of desorption temperature in comparison with Cu/CeO_2, which may be attributed to the interaction of NO with small Co_2O_3 or Co_3O_4 particles.[29] However, Fe addition has no obvious effect on desorption properties of NO. For $CuMn/CeO_2$, the peaks at 104 and 385 ^oC are related to desorption of NO and surface adsorbed nitrite/nitrate species, respectively. Interestingly, the peak intensity in CuM/CeO_2 is increased in comparison with that of Cu/CeO_2, suggesting that Fe, Co and Mn addition is favorable for NO adsorption at low temperature. The total desorption amounts of NO are in the following order: $CuMn/CeO_2$ > $CuCo/CeO_2$ > $CuFe/CeO_2$ > Cu/CeO_2 (Table 1). Compared to Cu/CeO_2, large NO desorption amount in CuM/CeO_2 is beneficial for promoting SCR activity at low temperature. To evaluate desorption species from NO-TPD, an online mass tracking was performed. The temperature-dependent mass profiles of $CuCo/CeO_2$ show that NO is the major product, trace amount of N_2O and NO_2 are also generated during NO desorption (Fig. 7b).

In order to investigate stability of mesoporous structures during SCR, TEM and HR-TEM analyses of Cu/CeO_2 and CuM/CeO_2 were carried out after SCR test. As shown in Fig. 8, TEM images show that mesoporous structures are still exist in the used Cu/CeO_2 and CuM/CeO_2, but Cu/CeO_2 shows slightly severe particle aggregation in comparison with CuM/CeO_2, suggesting the addition of Fe, Co and Mn may inhibit the growth of metal oxide particles.

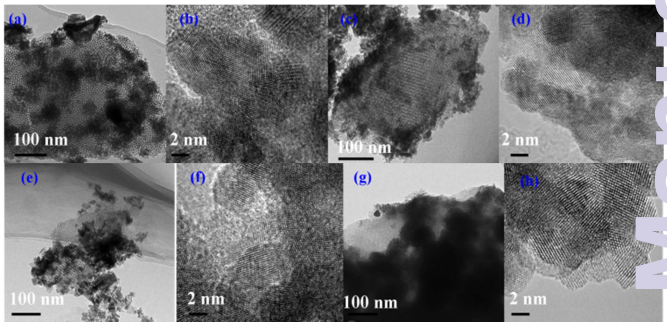

Fig. 8 TEM images after SCR test for (a) $CuCo/CeO_2$, (c) $CuMn/CeO_2$, (e) $CuFe/CeO_2$ and (g) Cu/CeO_2; HR-TEM of (b) $CuCo/CeO_2$, (d) $CuMn/CeO_2$, (f) $CuFe/CeO_2$ and (h) Cu/CeO_2.

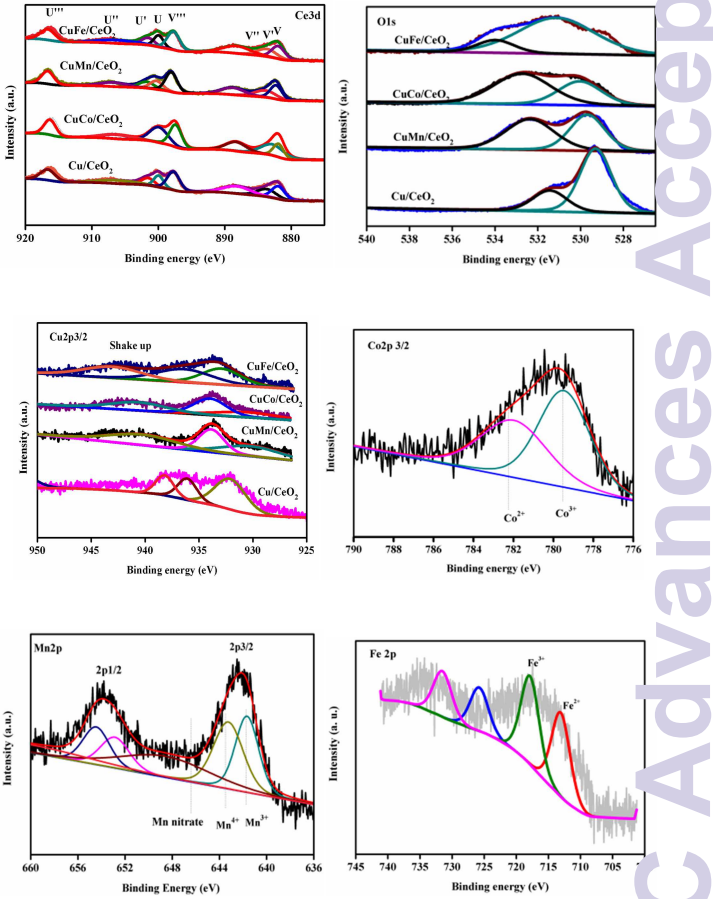

Fig. 9 XPS spectra of Ce3d, O1s, Cu2p, Co2p, Mn2p and Fe2p in Cu/CeO_2 and CuM/CeO_2.

The surface composition and chemical state of the elements in Cu/CeO_2 and CuM/CeO_2 were studied by XPS. As shown in Fig. 9, their Ce3d XPS spectra are decomposed into eight peaks, corresponding to four pairs of spin-orbit doublets. Following conventional fitting and labeling of the peaks,[21] $3d_{3/2}$ and $3d_{5/2}$ spin-orbit components are labeled as U and V, respectively. The peaks of U' and V' are assigned as Ce^{3+} species, while the other peaks correspond to Ce^{4+} species. The proportion of Ce^{3+} with regard to total cerium was calculated based on the area ratio of Ce^{3+} species. The values of Ce^{3+} species in total Ce are in the following sequence: $CuCo/CeO_2$ (28.94%) > $CuMn/CeO_2$ (26.89%) > $CuFe/CeO_2$ (10.59%). It is well known that Co species on Ce surface usually show multiple oxidation states, which may promote the reducibility of Ce^{4+} to Ce^{3+} by electron transfer, resulting in more Ce^{3+} species in $CuCo/CeO_2$.[32,33] In general, the presence of Ce^{3+} is associated with the formation of oxygen vacancies according to charge compensation. Therefore, the relative higher Ce^{3+} content in $CuCo/CeO_2$ indicates the formation of more oxygen vacancies. The decrement of Ce^{3+} content of $CuFe/CeO_2$ may be attributed to more stable 3d structure of Fe ions,[23] leading to low concentration of the exposed Ce^{3+} and oxygen vacancies, which is consistent with XRD and Raman results.

Table 2 Surface atomic ratio of Cu, Cu^{2+}/Cu, Cu^{+}/Cu, O_{ads}/O_{latt}, and Ce^{3+}/Ce.

Sample	Surface Cu	Cu^{2+}/Cu	Cu^{+}/Cu	O_{ads}/O_{latt}	Ce^{3+}/Ce
Cu/CeO_2	5.36	48.75	51.25	0.36	19.50
$CuMn/CeO_2$	3.73	49.24	50.76	1.18	26.84
$CuCo/CeO_2$	3.99	62.41	37.59	1.69	28.94
$CuFe/CeO_2$	4.93	53.70	46.30	0.19	10.59

It is well known that the formation of oxygen vacancies plays an important role in SCR of NO_x, which is helpful to the activation of oxygen species at the catalyst surface.[36] XPS spectra of O1s in Cu/CeO_2 and CuM/CeO_2 are also shown in Fig. 10, the low binding energy peak at 530.2 eV can be assigned to lattice oxygen,[38] while high peaks in Cu/CeO_2 and CuM/CeO_2 occur at 531.5 and 532.4-533.9 eV, respectively, corresponding to the surface-adsorbed oxygen species, which are derived from the adsorption of gaseous O_2 on the oxygen vacancies. The O_{ads}/O_{latt} ratio follows the trend: $CuFe/CeO_2$ < Cu/CeO_2 < $CuMn/CeO_2$ < $CuCo/CeO_2$ (Table 2), suggesting $CuCo/CeO_2$ possesses the most oxygen vacancies,

The surface concentration of Cu in CuM/CeO_2 is lower than that of Cu/CeO_2 (Table 2), which indicates that more Cu ions in CuM/CeO_2 are incorporated into ceria lattice to form solid soiution.[25] For XPS spectra of Cu $2p_{3/2}$, the peaks of binding energy with a maximum at 933.6 eV and a shake-up satellite at 942.1 eV indicate the presence of Cu^{2+}, while the peak at 932.8 eV is assigned to Cu^{+} species. Therefore, it can be deduced that CuO and Cu_2O are main Cu species at the catalyst surface.[15] The surface Cu^{2+}/Cu and Cu^{+}/Cu atomic ratios in CuM/CeO_2 are listed in Table 2. The Cu^{2+}/Cu ratio in $CuCo/CeO_2$ (62.41%) is higher than that of $CuFe/CeO_2$ (53.70%) and $CuMn/CeO_2$ (49.24%).

XPS spectrum of Co $2p_{3/2}$ in $CuCo/CeO_2$ shows two main peaks at 780.2 and 784.2 eV, which can be assigned to Co^{3+} and Co^{2+}, respectively.[22] XPS spectrum of Mn $2p_{3/2}$ in$CuMn/CeO_2$ indicates that MnO_2 (642.2 eV) and Mn_2O_3 (641.2 eV) are major phases. For XPS spectrum of Fe $2p_{3/2}$ in $CuFe/CeO_2$, two characteristic peaks at 713.07 and 717.86 eV correspond to Fe^{2+} and Fe^{3+}, respectively.

Conclusions

A series of the ordered mesoporous $Cu/CeO_2$and CuM/CeO_2 were prepared through nanocasting method. In comparison with mesoporous Cu/CeO_2, the additions of Fe, Co and Mn oxides have important effects on the textural and structural properties as well as SCR performances. Among them, $CuCo/CeO_2$ possesses superior catalytic activity, strong resistance against SO_2 and wide temperature window of 200-400 °C in SCR of NO_x with H_2. The superior SCR performances are associated with the surface CoO_x species, better reduction property of Ce^{4+} to Ce^{3+}, more oxygen vacancies and lower NO desorption temperature. In summary, this study has demonstrated that the ordered mesoporous $CuCo/CeO_2$ may serve as promising H_2-SCR catalysts at low temperature, which provides a new route for development of effective and cheap low-temperature SCR catalysts.

Acknowledgements

The work was supported by the State Key Project of Fundamental Research for Nanoscience and Nanotechnology (2011CBA00502, 2013CB933200), Major Project of Fujian Province (2013H0061).

Notes and references

1 C. K. Narula, L. F. Allard, G. M. Stocks and M. Moses-Debusk, *Sci. Rep.,* 2014, **4**, 7238.
2 U. Deka, I. Lezcano-Gonzalez, B. M. Weckhuysen and A. M. Beale, *ACS Catal.,* 2013, **3**, 413-427.
3 M. Colombo, I. Nova and E. Tronconi, *Appl. Catal. B: Environ.,* 2012, **111-112**, 433-444.
4 X. Mou, B. Zhang, Y. Li, L. Yao, X. Wei, D. Su and W. Shen. *Angew. Chem. Int. Ed.,* 2012, **51**, 2989-2993.
5 O. Mihai, C. R. Widyastuti, S. Andonov, K. Kamasamudram, J. Li, S. Y. Joshi, N. W. Currier, A. Yezerets and L. Olsson, *J. Catal.,* 2014, **311**,170-181.
6 P. M. More, N. Jagtap, A. B. Kulal, M. K. Dongare and S. Umbarkar, *Appl. Catal. B: Environ.,* 2014, **144**,408-415.
7 Y. Wan, W. Zhao, Y. Tang, L. Li, H. Wang, Y. Cui, J. Gu, Y. Li and J. Shi, *Appl. Catal. B: Environ.*, 2014, **148-149**, 114-122.
8 H. Chang, X. Chen, J. Li, L. Ma, C. Wang, C. Liu, J. W. Schwank and J. Hao, *Environ. Sci. Technol.,* 2013, **47**, 5294-5301.
9 Z. Liu, J. Li and S. I. Woo, *Energy Environ. Sci.,* 2012, **5**, 8798-8814.
10 C. N. Cost and A. M. Efstathiou, *Appl. Catal. B: Environ.,* 2007, **72**, 240-252.

11 L. Li, P. Wu, Q. Yu, G. Wu and N. Guan, *Appl. Catal. B: Environ.,* 2010, **94**, 254-262.
12 F. M. Auxilia, S. Ishihara, S. Mandal, T. Tanabe, G. Saravanan, G. V. Ramesh, N. Umezawa, T. Hara, Y. Yu and S. Hishita, *Adv. Mater.,* 2014, **26**, 4481-4485.
13 Z. Wang, Z. Qu, X. Quan, Z. Li, H. Wang and R. Fan, *Appl. Catal. B: Environ.,* 2013, **134-135**, 163-160.
14 P. Venkataswamy, D. Jampaiah, K. N. Rao and B. M. Reddy, *Appl.Catal. A: Gen.*, 2014, **488**, 1-10.
15 Z. Liu, S. Chai, A. Binder, Y. Li, L. Ji and S. Dai, *Appl. Catal. A: Gen.,* 2013, **451**, 282-288.
16 M. Turco, C. Cammarano, G. Bagnasco, E. Moretti, L. Storaro, A. Talon and M. Lenarda, *Appl. Catal. B: Environ.,* 2009, **91**, 101-107.
17 J. Zhu, Q. Gao and Z. Chen, *Appl. Catal. B: Environ.,* 2008, **81**, 236-243.
18 E. S. Gnanakumar, J. M.Naik, M. Manikandan, T.Raja and C. S. Gopinath, *ChemCatChem,* 2014, **6**, 3116-3124
19 C. R. Jung, A. Kundu, S. W. Nam and H-I. Lee, *Appl. Catal. B: Environ.,*2008, **84**,426-432.
20 (a) F. Jiao, A. H. Hill, A. Harrison, A. Berko, A. V. Chadwick and P. G. Bruce, *J. Am. Chem. Soc.,* 2008, **130**, 5262-5266.
21 Y. J. Sa, K. Kwon, J. Y. Cheon, F. Kleitz and S. H. Joo, *J. Mater. Chem. A.,* 2013, **1**, 9992-10001.
22 X. Wang, L. Jiang, J. Wang and R. Wang, *Appl. Catal. B: Environ.,* 2015,**165**, 700-705.
23 S. Wang, N. Li, L. Luo, W. Huang, Z. Pu, Y. Wang, G. Hu, M. Luo and J. Lu, *Appl. Catal. B: Environ.,* 2014, **144**, 325-332.
24 C. Tang, J. Sun. X. Yao, Y. Cao, L. Liu, C. Ge, F. Gao and L. Dong, *Appl. Catal. B: Environ.,* 2014, **146**, 201-212.
25 J. Li, Y. Han, Y. Zhu and R. Zhou, *Appl. Catal. B: Environ.,* 2011, **108-109**, 72-80.
26 J. Liu, Z. Zhao, J. Wang, C. Xu, A. Duan, G. Jiang and Q. Yang, *Appl. Catal. B: Environ*., 2008, **84**, 185-195.
27 Z. Zhang, D. Han, S. Wei and Y. Zhang, *J. Catal.,* 2010,**276**,16-23.
28 Z. Li, L. Li, Q. Yuan, W. Feng, J. Xu, L. Sun, W. Song and C. Yan, *J. Phys. Chem. C,* 2008, **112**, 18405-18411.
29 Y. Feng, L. Li, S. Niu, Y. Qu, Q. Zhang, Y. Li, W. Zhao, H. Li and J. Shi, *Appl. Catal. B: Environ.,* 2012,**111-112**, 461-466.
30 J. Rosen, G. S. Hutchings and F. Jiao, *J. Catal.,* 2014, **310**,2-9.
31 J. Li, P. Zhu, S. Zuo, Q. Huang and R. Zhou, *Appl. Catal. A: Gen.,* 2010, **381**, 261-266;
32 J. Beckers and G. Rothenberg, *Dalton Trans.*, 2008, 6573-6578;
33 T. Mathew, K. Sivaranjani, E. S. Gnanakumar, Y. Yamada, T. Kobayashi and C. S. Gopinath, *J. Mater Chem.*, 2012, **22**, 13484-13493.
34 X. Yao, F. Gao, Y. Cao, C. Tang, Y. Deng, L. Dong and Y. Chen, *Phys. Chem. Chem. Phys.,* 2013, **5**, 14945-14950.
35 K. Li, M. Haneda, Z. Gu, H. Wang and M. Ozawa, *Materials Lett.,* 2013, **93**, 129-132.
36 R. Moreno-Tost, J. Santamaría-González, P. Maireles-Torres, E. Rodríguez-Castellón and A. Jiménez-López, *J. Mater. Chem.,* 2002, **12**, 3331-3336.
37 P. Dutta, S. Pal and M. S. Seehra, *Chem. Mater.,* 2006, **18**, 5144-5146.
38 S. Cai, D. Zhang, L. Shi, J. Xu, L. Zhang, L, Huang, H. Li and J. Zhang, *Nanoscale,* 2014, **6**, 7346-7353.